

Controlling inertial active Brownian motion via stochastic resetting

Manish Patel^{1,2,*} and Amir Shee^{3,†}

¹*Institute of Physics, Sachivalaya Marg, Bhubaneswar, Odisha 751005, India*

²*Homi Bhabha National Institute, Anushakti Nagar, Mumbai, Maharashtra 400094, India*

³*Department of Physics, University of Vermont, Burlington, Vermont 05405, USA*

(Dated: February 25, 2026)

Inertia is intrinsic to many living and synthetic active systems, from animals and robotic agents to colloidal swimmers, and it strongly shapes transport. Many such systems employ intermittent restart protocols to regulate exploration. Stochastic resetting provides a theoretical framework for these strategies and a route to control nonequilibrium steady states, yet the role of inertia in reset-controlled active dynamics remains poorly understood. Here we study an inertial active Brownian particle subject to complete stochastic resetting of position, velocity, and orientation in two dimensions. Using a moment-generating framework together with the Final-Value Theorem, we derive closed-form steady-state moments up to fourth order as functions of inertia, activity, and reset rate. We show that inertia fundamentally modifies reset-controlled transport: at large reset rates the steady-state mean-squared displacement is suppressed much more strongly than in the overdamped limit, yielding enhanced localization near the reset point. At the same time, position excess-kurtosis phase diagrams reveal strongly non-Gaussian steady states characterized by a sharp central peak coexisting with heavy tails in the position distribution, indicating rare long excursions enabled by inertial persistence. The tail weight varies non-monotonically with reset rate, reflecting a competition between inertial momentum relaxation and resetting that selects an optimal regime maximizing rare excursions. Our results provide experimentally testable signatures of inertial effects in reset-controlled active systems.

I. INTRODUCTION

Efficient navigation is a fundamental challenge for active agents, both living and synthetic, operating in noisy and structured environments [1–4]. From foraging organisms to microrobots, effective motion requires balancing extensive exploration with reliable return, while operating under finite time and energetic constraints [5–7]. A powerful and widely observed strategy to regulate this balance is to intermittently interrupt motion and reset key state variables, thereby limiting unproductive excursions and maintaining control over spatial exploration. This restart mechanism, formalized as stochastic resetting, provides a general framework for controlling search dynamics and has emerged as a unifying principle across physical, chemical, and biological systems [8–15].

Stochastic resetting provides a theoretical framework for restart protocols [8, 9], in which the dynamics is interrupted at random times and returned to a prescribed state, thereby preventing indefinite wandering and producing well-defined nonequilibrium steady states [16–18]. Resetting can reduce first-passage times, enhance search efficiency, and tune steady-state fluctuations in both passive and active systems [19–25]. For active particles, however, most existing work has focused on overdamped dynamics, where inertia is neglected and the velocity is effectively slaved to the propulsion direction [22, 26–28]. This limit is not appropriate for many experimentally relevant settings, including low-damping colloids,

vibrated granular particles, self-propelled robots, and animal locomotion, where inertia plays an essential dynamical role [29–40]. Finite inertia introduces a momentum-relaxation timescale that delays the response of the velocity to changes in orientation and can qualitatively reshape transport and fluctuation statistics [41–47]. Despite this, steady-state statistics of inertial active particles under stochastic resetting, including the emergence of non-Gaussian fluctuations that control exploration and localization, remain largely unexplored.

Here, we analyze the steady state of an inertial active Brownian particle subject to complete stochastic resetting of position, velocity, and orientation. We focus on translational inertia, assuming that rotational inertia relaxes rapidly and can be neglected, although it may play an important role in active colloids and related systems [48–50]. Using a moment-generating framework [44, 45, 51–54] combined with the Final-Value Theorem, we derive closed-form steady-state expressions for second- and fourth-order moments across the full parameter space of inertia M , Péclet number Pe (activity), and reset rate r . We use the excess kurtosis as our primary metric and find that inertia fundamentally reshapes reset-driven transport and fluctuations.

The steady-state mean-squared velocity (MSV) $\langle \mathbf{v}^2 \rangle_r^{\text{st}}$ decreases with increasing inertia, scaling as M^{-1} in the absence of resetting [44]. With stochastic resetting, the MSV exhibits the same scaling at low inertia but is more strongly suppressed at large inertia, where $\langle \mathbf{v}^2 \rangle_r^{\text{st}} \sim M^{-2}$. As a function of the reset rate, the MSV remains approximately constant at low r and decays at large r as $\langle \mathbf{v}^2 \rangle_r^{\text{st}} \sim r^{-1}$. The steady-state mean-squared displacement (MSD) $\langle \mathbf{r}^2 \rangle_r^{\text{st}}$ is nearly independent of inertia at low

* contact author: manish.patel@iopb.res.in

† contact author: amir.shee@uvm.edu

M but is strongly suppressed at high inertia, scaling as $\langle \mathbf{r}^2 \rangle_r^{\text{st}} \sim M^{-2}$. In the overdamped limit, the MSD decreases with the reset rate as $\langle \mathbf{r}^2 \rangle_r^{\text{st}} \sim r^{-1}$ [55], a scaling that persists at low reset rates for inertial active Brownian particles. In contrast, at large reset rates the suppression is much stronger, with $\langle \mathbf{r}^2 \rangle_r^{\text{st}} \sim r^{-3}$. Notably, all these asymptotic exponents are activity-independent: passive particles exhibit the same asymptotic behavior, differing only in quantitative amplitudes.

The steady-state second-order moments exhibit clear qualitative and quantitative differences in the presence of inertia, reflecting a pronounced suppression of steady-state fluctuations. To further quantify the emergence of heavy-tailed statistics, we use the excess kurtosis as a primary metric and construct phase diagrams in the (M, r) plane. These reveal broad regimes of strong non-Gaussianity and re-entrant behavior arising from the competition between persistence, momentum relaxation, and reset frequency. Together, these results show that inertia is a key control variable in reset-controlled active systems: it sharpens typical localization at large reset rates while amplifying rare excursions, thereby enriching steady-state fluctuation statistics and producing tunable non-Gaussian steady states. The analytical structure uncovered here provides a compact baseline for experiments in colloidal, granular, and robotic platforms and opens pathways toward reset-informed navigation and sampling protocols in autonomous active agents [37–40].

The paper is organized as follows. In Sec. II we introduce the inertial active Brownian particle model with complete stochastic resetting and define the dimensionless control parameters (M, Pe, r) . In Sec. III we present exact steady-state second moments of velocity and displacement and summarize their limiting behavior. In Sec. IV we present kurtosis-based phase diagrams in the (M, r) plane and relate them to the underlying steady-state distributions, highlighting inertial re-entrant behavior and heavy-tailed regimes. Section V concludes with a discussion of implications and outlook.

II. MODEL

We study an inertial active Brownian particle in two dimensions under complete stochastic resetting. It is characterized by its position $\mathbf{r} = (x, y)$, velocity $\mathbf{v} = (v_x, v_y)$, and its orientation (or heading direction) $\hat{\mathbf{u}} = (u_x, u_y)$, which is a unit vector in two dimensional plane where $u_x = \cos(\theta)$ and $u_y = \sin(\theta)$, evolving over time t in the presence of thermal noise at temperature T satisfying the fluctuation-dissipation relation. We define the translational diffusion coefficient as $D \equiv k_B T / \gamma$. We impose complete stochastic resetting on \mathbf{r} , \mathbf{v} , and $\hat{\mathbf{u}}$, allowing the intermittent resets to the reset states $(\mathbf{r}_0, \mathbf{v}_0, \hat{\mathbf{u}}_0)$ with rate r_0 . Between reset events, the particle self-propels along $\hat{\mathbf{u}}$ while its velocity relaxes on a finite momentum-relaxation time (Fig. 1(a)). This protocol establishes a nonequilibrium steady state for

$r_0 > 0$ in which excursions between resets are repeatedly “restarted,” enabling direct control of localization and excursions through r_0 .

The position \mathbf{r} , velocity \mathbf{v} , and orientation angle θ evolution in 2-dimensions can be written as

$$d\mathbf{r} = \mathbf{v} dt, \quad (1)$$

$$m d\mathbf{v} = -\gamma(\mathbf{v} - v_0 \hat{\mathbf{u}}) dt + \sqrt{2\gamma k_B T} d\mathbf{B}^t(t), \quad (2)$$

$$d\theta = \sqrt{2D_r} dB^r(t) \quad (3)$$

$$(\mathbf{r}, \mathbf{v}, \theta) \rightarrow (\mathbf{r}_0, \mathbf{v}_0, \theta_0). \quad (4)$$

The dynamics is illustrated schematically in Fig. 1(a). The noise terms $d\mathbf{B}^t$ and dB^r are modeled as Gaussian white noise with zero mean and variances given by $\langle dB_i^t dB_j^t \rangle = \delta_{ij} dt$ and $\langle dB^r dB^r \rangle = dt$, respectively. The dynamics of the inertial active Brownian particle under stochastic resetting is governed by Eqs. (1)–(4). We assume the origin of the active orientational dynamics to be independent of inertia [44, 45]. Eq. (4) implements complete resetting of position, velocity, and orientation. This inertial coupling implies that \mathbf{v} does not instantaneously align with $\hat{\mathbf{u}}$ (Fig. 1(b)): after a change of heading the velocity responds with a finite delay set by inertia. While in this work we focus on complete resetting, other protocols are also possible, such as resetting position together with velocity, velocity alone, or resetting to random states, each of which would generate distinct nonequilibrium steady states [22, 26, 28].

We analyze the model in dimensionless units by measuring time in units of the rotational persistence time $\tau_r = 1/D_r$ and length in units of $\ell = \sqrt{D/D_r}$. We present all results in dimensionless form by rescaling position as $\mathbf{r} \rightarrow \mathbf{r}/\ell$, time as $t \rightarrow t/\tau_r$, and velocity as $\mathbf{v} \rightarrow \mathbf{v}/\sqrt{DD_r}$. Three dimensionless parameters fully control the dynamics: (i) the *inertia* $M = \tau/\tau_r$ with $\tau = m/\gamma$ the momentum-relaxation time; (ii) the *activity* (Péclet number) $\text{Pe} = v_0/\sqrt{DD_r}$, which sets the strength of self-propulsion; and (iii) the *reset rate* $r = r_0\tau_r$, which sets the average duration of each excursion. In this reduced description, “overdamped” motion corresponds to $M \rightarrow 0$ (instantaneous velocity response), while $M \gg 1$ represents the strongly inertial regime with pronounced velocity–orientation lag (Fig. 1(b)). This delay directly impacts single-particle trajectories under resetting (Fig. 1(c)). At fixed $r = 1$ and $\text{Pe} = 10$, weakly inertial particles ($M = 0.01$) closely track the propulsion direction, whereas increasing inertia ($M = 1$) induces relatively smooth (less fluctuating; Fig. 1(c)) trajectories between resets. Figure 1(d) illustrates that inertia qualitatively reshapes the steady-state spatial distribution under stochastic resetting: the density becomes increasingly concentrated near the reset position as M increases.

The velocity dynamics of a free inertial ABP [44] can be viewed as mathematically equivalent to the position dynamics of an overdamped ABP in a harmonic trap [53], with momentum relaxation playing the role of trap stiffness (see Appendix A). As a result, under stochastic resetting the velocity statistics of the inertial particle follow

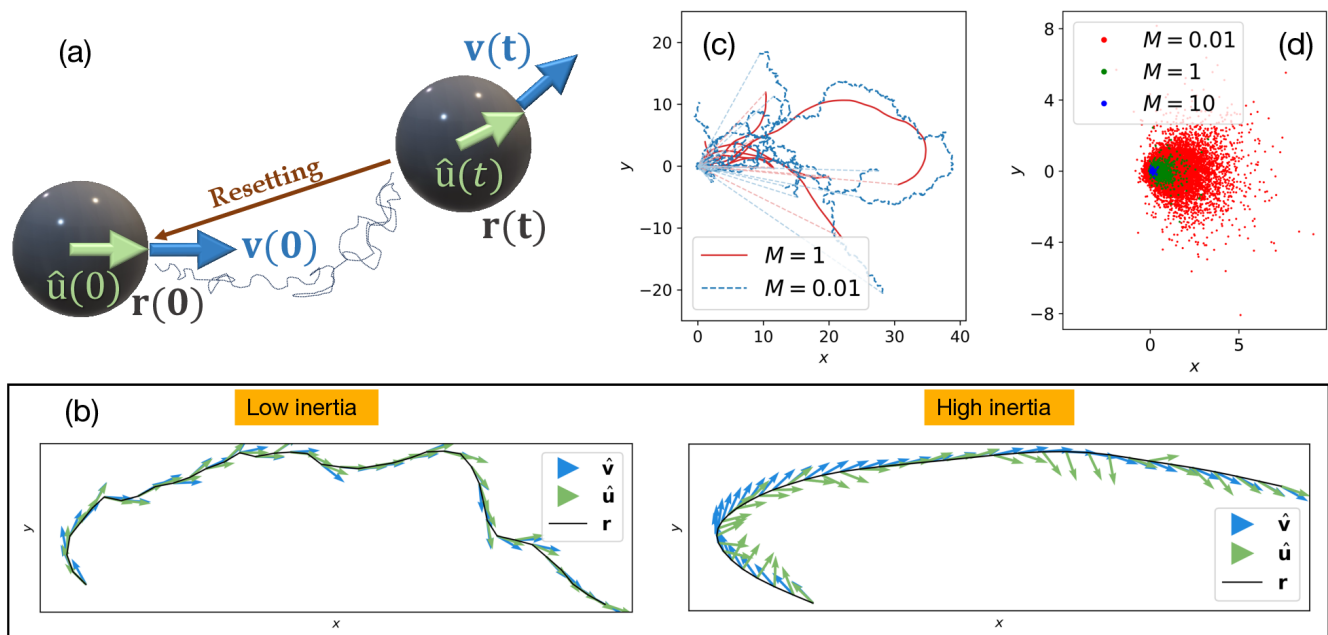


FIG. 1. Inertial effects in active Brownian particles under stochastic resetting. (a) Schematic diagram of the inertial active Brownian particle position \mathbf{r} , velocity \mathbf{v} , and orientation $\hat{\mathbf{u}}$ evolve (see Eqs. (1)–(4)), with intermittent complete resetting to the initial state $(\mathbf{r}(0), \mathbf{v}(0), \hat{\mathbf{u}}(0)) \equiv (\mathbf{r}_0, \mathbf{v}_0, \hat{\mathbf{u}}_0)$. (b) In the overdamped regime (low inertia), the particle exhibits an instantaneous orientational response: velocity direction $\hat{\mathbf{v}}$ is immediately slaved to the propulsion direction $\hat{\mathbf{u}}$. In the underdamped regime (high inertia), the particle shows a delayed response, where velocity direction $\hat{\mathbf{v}}$ relaxes over a finite time due to inertia. (c) Comparison of steady state single particle trajectory for inertia $M = 0.01$ and 1 at reset rate $r = 1$ and activity $\text{Pe} = 10$. (d) Steady state positions snapshot of 2×10^4 particles for inertia $M = 0.01, 1,$ and 10 at reset rate $r = 10$ and activity $\text{Pe} = 10$. We consider the initial (reset) state $\mathbf{r}_0 = 0, \mathbf{v}_0 = 0,$ and $\hat{\mathbf{u}}_0 = (1, 0)$.

those of a trapped overdamped active particle with the appropriate parameter mapping [55]. In contrast, the position of an inertial active particle does not admit such a simple correspondence as it remains coupled to velocity, leading to novel reset-induced behavior.

We set the initial and reset position of the particle at the origin, with zero velocity and orientation along the x axis: $(x, y, v_x, v_y, \theta) = (0, 0, 0, 0, 0)$. The stochastic dynamics defined by Eqs. (1)–(3) are simulated by discretizing the inertial Langevin equations with a time step Δt . The velocity update follows an underdamped Langevin scheme, while the particle orientation evolves according to rotational diffusion. We employ stochastic Euler-Maruyama for orientation and velocity–Verlet algorithm for position and velocity, which provides superior numerical stability and accuracy for inertial active systems. After each time step, the state $(\mathbf{r}, \mathbf{v}, \hat{\mathbf{u}})$ is reset to $(\mathbf{r}_0, \mathbf{v}_0, \hat{\mathbf{u}}_0)$ with probability $r\Delta t$. We derive exact closed-form steady-state expressions for moments up to fourth order using the moment-generating framework [44, 51–53], as detailed in Appendices B–D. In the main text, we analyze these results to characterize the steady-state fluctuation statistics.

III. SECOND ORDER MOMENTS

Mean-squared velocity (MSV). The steady-state mean-squared velocity (MSV) of an inertial active Brownian particle under complete stochastic resetting is given by (see Appendix C for derivation)

$$\langle \mathbf{v}^2 \rangle_r^{\text{st}} = \frac{2}{2 + Mr} \left(\frac{2}{M} + \frac{\text{Pe}^2}{1 + M(1 + r)} \right). \quad (5)$$

This expression is formally identical to the steady-state MSD of an overdamped ABP under resetting [55] via the mapping (see Appendix A). In the absence of resetting ($r = 0$), one recovers the known result for free inertial ABPs [44], $\langle \mathbf{v}^2 \rangle^{\text{st}} = 2/M + \text{Pe}^2/(1 + M)$, which reduces to the Brownian limit $\langle \mathbf{v}^2 \rangle^{\text{st}} = 2/M$ for $\text{Pe} = 0$ [56] (Fig. 2(a,b)). For weak resetting, the MSV is nearly independent of r for both active and passive particles (Fig. 2(b)). In the passive limit ($\text{Pe} = 0$), Eq. (5) reduces to

$$\langle \mathbf{v}^2 \rangle_r^{\text{st}} = \frac{4}{M(2 + Mr)}, \quad (6)$$

showing that stochastic resetting steepens the large- M scaling from M^{-1} (free inertial Brownian motion [56])

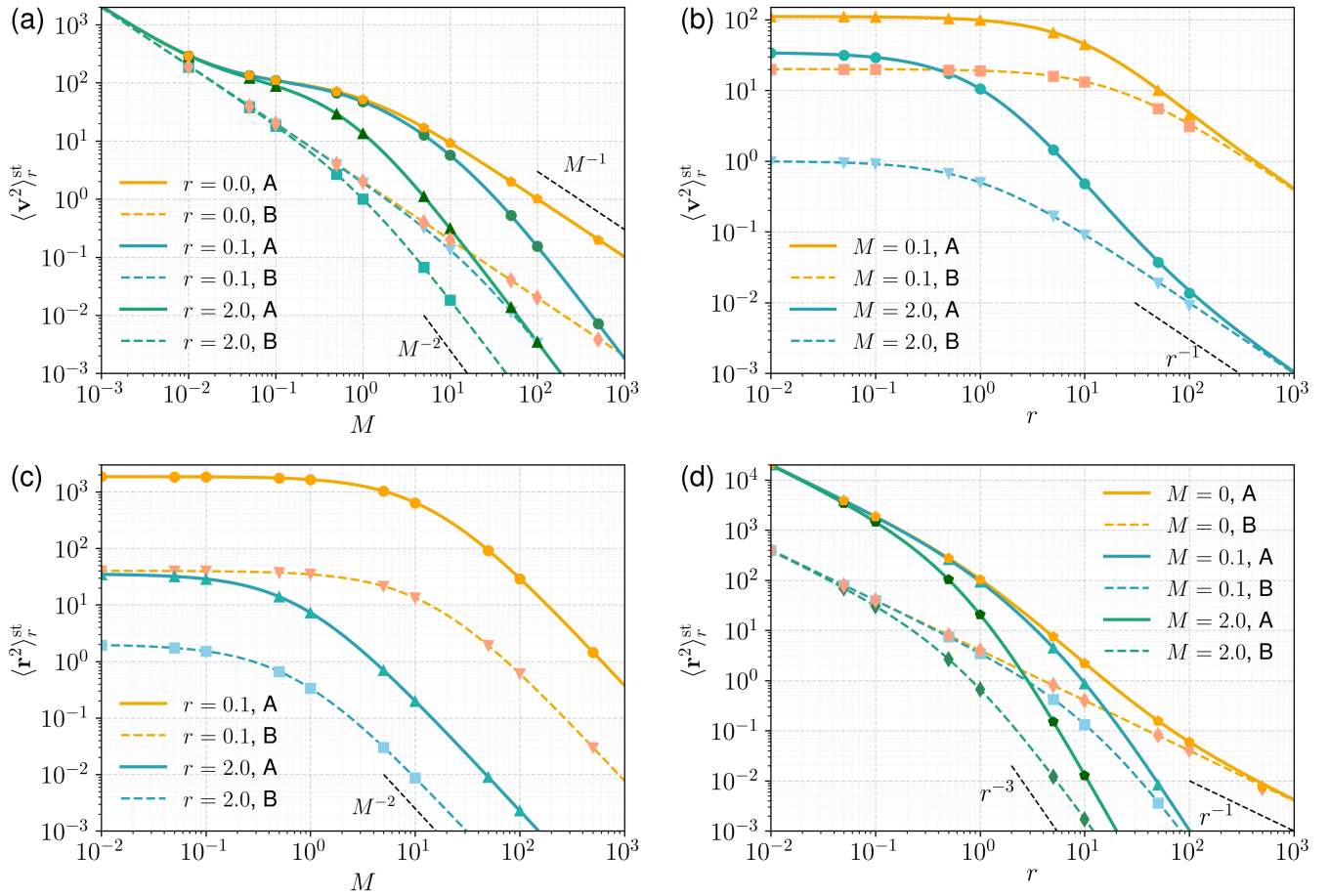


FIG. 2. Steady-state second moments under stochastic resetting. (a,b) Mean-squared velocity (MSV) and (c,d) mean-squared displacement (MSD) of inertial active Brownian particles under complete stochastic resetting. Active particles ($Pe = 10$, solid lines, labelled A) are compared with passive Brownian particles ($Pe = 0$, dashed lines, labelled B). (a) MSV as a function of inertia M for reset rates $r = 0, 0.1, 2.0$. (b) MSV as a function of reset rate r for $M = 0.1, 2.0$. (c) MSD as a function of inertia M for $r = 0.1, 2.0$. (d) MSD as a function of reset rate r for $M = 0$ (overdamped), 0.1 , and 2.0 . Lines denote analytical predictions; symbols represent simulation data. Inertia and resetting suppress steady-state fluctuations, while activity enhances both MSV and MSD relative to the passive baseline.

TABLE I. Limiting cases and asymptotic scaling of the steady-state mean-squared displacement (MSD) $\langle \mathbf{r}^2 \rangle_r^{\text{st}}$ and mean-squared velocity (MSV) $\langle \mathbf{v}^2 \rangle_r^{\text{st}}$ for different limits of inertia M and reset rate r . “NO SS”: no steady state; “NA”: not defined in the overdamped limit. Scaling statements refer to asymptotic limits at fixed remaining parameters.

Limit	MSD $\langle \mathbf{r}^2 \rangle_r^{\text{st}}$	MSV $\langle \mathbf{v}^2 \rangle_r^{\text{st}}$
No reset ($r = 0$) [44]	NO SS	$\frac{2}{M} + \frac{Pe^2}{1+M}$
Overdamped Brownian ($M = 0, Pe = 0$) [55]	$\frac{4}{r}$	NA
Overdamped ABP ($M = 0$) [55]	$\frac{4}{r} + \frac{2Pe^2}{r(1+r)}$	NA
Underdamped Brownian ($Pe = 0$)	$\frac{4}{r(1+Mr)(2+Mr)}$	$\frac{4}{M(2+Mr)}$
Our model: low reset rate	$\sim r^{-1}$ (as in overdamped)	$\langle \mathbf{v}^2 \rangle_{r=0}^{\text{st}}$ [44]
Our model: high reset rate	$\sim r^{-3}$ (as in passive Brownian)	$\sim r^{-1}$ (as in passive Brownian)
Our model: low inertia	$\langle \mathbf{r}^2 \rangle_r^{\text{st}}(M = 0)$ [55]	$\sim M^{-1}$ (as in $r = 0$ limit)
Our model: high inertia	$\sim M^{-2}$ (as in passive Brownian)	$\sim M^{-2}$ (as in passive Brownian)

to M^{-2} , reflecting enhanced suppression of velocity fluctuations (Fig. 2(a)). At large reset rates, the MSV de-

cays universally as $\langle \mathbf{v}^2 \rangle_r^{\text{st}} \sim r^{-1}$, independent of activity (Fig. 2(b)). Note that in the passive limit ($\text{Pe} = 0$), τ_r acts only as a reference time scale for nondimensionalization; all dimensional observables are independent of τ_r . The dimensional MSV in passive limit is $\langle \tilde{\mathbf{v}}^2 \rangle_r^{\text{st}} = (l/\tau_r)^2 \langle \mathbf{v}^2 \rangle_r^{\text{st}} = 4D/[\tau(2 + \tau r_0)]$.

Mean-squared displacement (MSD). The steady-state mean-squared displacement (MSD) of an inertial active Brownian particle under complete stochastic resetting is (see Appendix C for derivation)

$$\langle \mathbf{r}^2 \rangle_r^{\text{st}} = \frac{2}{r(1 + Mr)(2 + Mr)} \times \left[4 + \frac{\text{Pe}^2(2 + 2M + 3Mr)}{(r + 1)(1 + M + Mr)} \right]. \quad (7)$$

In the passive limit ($\text{Pe} = 0$), Eq. (7) reduces to the exact result for underdamped Brownian motion under resetting,

$$\langle \mathbf{r}^2 \rangle_r^{\text{st}} = \frac{8}{r(1 + Mr)(2 + Mr)}. \quad (8)$$

For overdamped Brownian motion, the steady-state MSD decays as $\langle \mathbf{r}^2 \rangle_r^{\text{st}} = 4/r$ [55]. The presence of inertia suppresses the MSD for all $r > 0$ and leads to a markedly faster asymptotic decay at large reset rates, $\langle \mathbf{r}^2 \rangle_r^{\text{st}} \sim 8/(M^2 r^3)$ as $r \rightarrow \infty$ (Fig. 2(c,d)). Thus, inertia enhances localization under resetting while simultaneously limiting long excursions and large-scale exploration. The asymptotic scaling of the second moments in the relevant limiting regimes is summarized in Table I. To construct the phase diagrams, we compute the steady-state fourth-order moments (see Appendix Fig. 5) and quantify deviations from Gaussian statistics using the excess kurtosis. To connect these phase diagrams to the underlying probability distributions, we compare the measured distributions with the corresponding Gaussian distributions constructed from the exact second-order moments.

IV. PHASE DIAGRAMS

Excess kurtosis as primary metric. We use the steady-state excess kurtosis as the primary metric to construct phase diagrams for both velocity and position statistics. For a zero-mean Gaussian process, $\langle \mathbf{r} \rangle_r^{\text{st}} = \langle \mathbf{v} \rangle_r^{\text{st}} = 0$, the fourth moments satisfy $(\mu_4^r)_{\mathbf{r}}^{\text{st}} = 2(\langle \mathbf{r}^2 \rangle_r^{\text{st}})^2$ and $(\mu_4^r)_{\mathbf{v}}^{\text{st}} = 2(\langle \mathbf{v}^2 \rangle_r^{\text{st}})^2$. We therefore define

$$\mathcal{K}_r^{\text{st}} = \frac{\langle \mathbf{r}^4 \rangle_r^{\text{st}}}{(\mu_4^r)_{\mathbf{r}}^{\text{st}}} - 1, \quad \mathcal{L}_r^{\text{st}} = \frac{\langle \mathbf{v}^4 \rangle_r^{\text{st}}}{(\mu_4^r)_{\mathbf{v}}^{\text{st}}} - 1, \quad (9)$$

which quantify departures from Gaussian steady-state statistics for position and velocity, respectively. We evaluate $\mathcal{K}_r^{\text{st}}$ and $\mathcal{L}_r^{\text{st}}$ analytically by combining the exact steady-state second moments (Eqs. (5) and (7)) with the

corresponding steady-state fourth moments (Eqs. (D15) and (D16)) derived in Appendix D. The resulting closed-form expressions for the excess kurtosis are algebraically lengthy. Instead, we use them to generate the phase-diagram heat maps and representative cuts, shown in Figs. 3(a–d) and 4(a–d). In what follows, we summarize the limiting behaviors and highlight the qualitative regimes that emerge.

Velocity excess kurtosis. In the zero activity limit, the steady-state velocity excess kurtosis reduces to the underdamped Brownian result

$$\lim_{\text{Pe} \rightarrow 0} \mathcal{L}_r^{\text{st}} = \frac{Mr}{4 + Mr}, \quad (10)$$

which is strictly positive (Fig. 3(a)). Equation (10) shows that non-Gaussianity is controlled solely by the dimensionless product Mr , which compares the momentum relaxation time to the mean resetting time. In the absence of resetting ($r = 0$), $\mathcal{L}_r^{\text{st}} = 0$ and the velocity distribution is Gaussian. In the overdamped limit ($M \rightarrow 0$), the resetting protocol does not affect velocity statistics, consistent with the rapid equilibration of \mathbf{v} relative to the other dynamical time scales. Increasing either inertia or reset rate enhances deviations from Gaussianity, with $\mathcal{L}_r^{\text{st}}$ rising monotonically and saturating to unity as $Mr \rightarrow \infty$ (Fig. 3(a)). Figure 3(a) presents the corresponding phase diagram in the (r, M) plane. The dashed line $Mr = 4$ marks the contour $\mathcal{L}_r^{\text{st}} = 1/2$, separating weakly and strongly non-Gaussian regimes. The analytical prediction (Eq. (10), lines) is in quantitative agreement with simulations (symbols) (Fig. 3(c,d)), and the distributions of $|\mathbf{v}|$ confirm a progressive enhancement of heavy tails with increasing Mr (Fig. 3e–j).

For finite activity ($\text{Pe} = 10$), the phase diagram reveals two re-entrant regimes: one emerging at low reset rates and the other in the strongly inertial limit (Fig. 3b). In the small resetting limit ($r \rightarrow 0$), the steady-state velocity excess kurtosis reduces to the known result for free inertial active Brownian particles [44]:

$$\lim_{r \rightarrow 0} \mathcal{L}_r^{\text{st}} = -\frac{\text{Pe}^4 M^2 (3 + 7M)}{2(3 + M)(1 + 2M)[2 + (2 + \text{Pe}^2)M]^2}. \quad (11)$$

This expression is strictly negative (Fig. 3b), consistent with the non-Gaussian velocity statistics of free active Brownian particles discussed in Ref. [44]. As a function of inertia M , the excess kurtosis $\mathcal{L}_{r \rightarrow 0}^{\text{st}}(M, \text{Pe})$ exhibits a non-monotonic, re-entrant dependence. In the overdamped limit ($M \rightarrow 0$), the excess kurtosis vanishes, reflecting Gaussian velocity statistics. With increasing inertia, deviations from Gaussianity are amplified, leading to a finite negative minimum at an activity-dependent value $M = M_*(\text{Pe})$. The location of this minimum follows from extremizing Eq. (11) with respect to M , yielding the quartic condition

$$7(\text{Pe}^2 + 2)M^4 + (6\text{Pe}^2 - 2)M^3 - 98M^2 - 84M - 18 = 0, \quad (12)$$

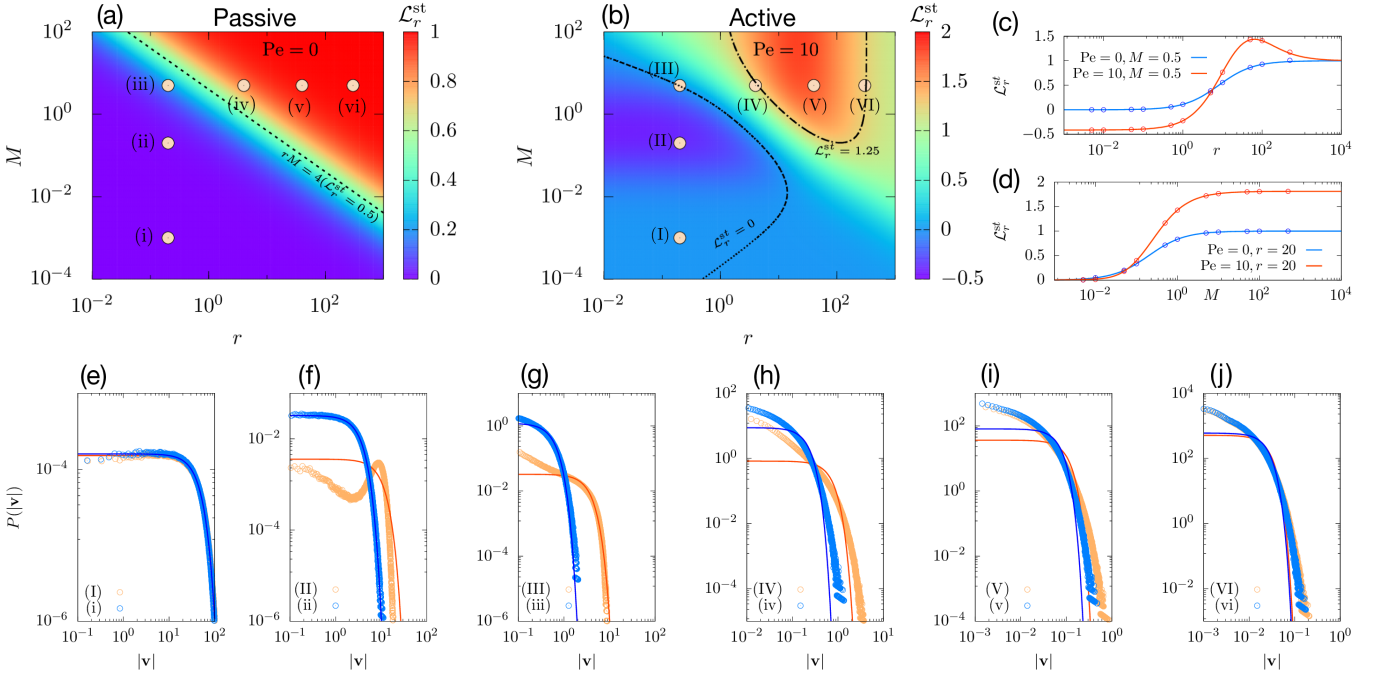


FIG. 3. Phase diagrams using velocity excess kurtosis as primary metric. Steady state excess kurtosis of velocity $\mathcal{L}_r^{\text{st}}$. Heat map in $r - M$ plane of (a) passive inertial Brownian particle under resetting $\text{Pe} = 0$, (b) inertial ABP under resetting. The line plot of excess kurtosis in velocity as a function of r in (c) and M in (d) at representative parameter values (lines: theory; symbols: simulations). The dashed line plot $rM = 4$ in (a) represents the line where $\mathcal{L}_r^{\text{st}} = 0.5$ and the dashed line in (b) corresponds to $\mathcal{L}_r^{\text{st}} = 0$. Probability distribution for magnitude of velocity $|v| = \sqrt{v_x^2 + v_y^2}$. (e)–(j) show the steady-state probability distributions of the velocity magnitude $|v|$ at selected points (i)–(vi) in the phase diagram in (a) and (I)–(VI) in the phase diagram in (b), illustrating how inertia and resetting jointly enhance heavy-tailed velocity fluctuations.

whose unique positive root defines $M_*(\text{Pe})$. For weak activity, $M_*(\text{Pe}) \simeq 3.09 - 0.90\text{Pe}^2 + \mathcal{O}(\text{Pe}^4)$, whereas for strong activity it decreases asymptotically as $M_*(\text{Pe}) \sim 3^{1/3}\text{Pe}^{-2/3}$. Thus, the inertia at which non-Gaussianity is maximal decreases monotonically with increasing activity. For sufficiently large inertia, the excess kurtosis relaxes back towards zero, with the asymptotic behaviour $\mathcal{L}_{r \rightarrow 0}^{\text{st}} \sim -c/M + \mathcal{O}(M^{-2})$ as $M \rightarrow \infty$, where $c = 7\text{Pe}^4/[4(2 + \text{Pe}^2)^2]$. Consequently, non-Gaussian effects are strongest at intermediate inertia, while both the overdamped and strongly inertial limits recover nearly Gaussian velocity statistics.

In the strongly inertial regime ($M \rightarrow \infty$), expanding around small reset rate ($r \rightarrow 0$)

$$\lim_{r \rightarrow 0} \lim_{M \rightarrow \infty} \mathcal{L}_r^{\text{st}} = 1 + \frac{\text{Pe}^2(\text{Pe}^2 + 16)}{4(\text{Pe}^2 + 2)^2} r + \mathcal{O}(r^2),$$

the excess kurtosis rises above unity at small r , reaches a single maximum at $r = r_*(\text{Pe})$, and then decreases monotonically back to 1 as $r \rightarrow \infty$ with the asymptotic scaling

$$\lim_{r \rightarrow \infty} \lim_{M \rightarrow \infty} \mathcal{L}_r^{\text{st}} = 1 + \frac{\text{Pe}^2}{r} + \mathcal{O}(r^{-2}).$$

Physically, optimizing over r balances frequent resets

(which suppress heavy tails) against activity-induced drive; the balance shifts to larger r as activity increases, but the excess kurtosis remains bounded, saturating below 2. Thus, as a function of resetting rate, the large-inertia excess kurtosis exhibits a re-entrant trend (Fig. 3(b)): it begins at unity, increases to a finite peak, and then relaxes back to unity under strong resetting. The analytical prediction (Eq. (9), lines) is in excellent agreement with simulations (symbols) (Fig. 3(c,d)), and the distributions of $|v|$ confirm re-entrant transitions (Fig. 3(e-j)). We summarize different limits and their velocity excess kurtosis behavior in Table II.

Position excess kurtosis. In the zero activity limit, the excess kurtosis of position reduces to

$$\lim_{\text{Pe} \rightarrow 0} \mathcal{K}_r^{\text{st}} = 19 + \frac{54}{3 + Mr} - \frac{144}{4 + Mr}. \quad (13)$$

which is strictly positive for all physical values of M and r . In the weak-resetting or low-inertia limit ($Mr \rightarrow 0$), the excess kurtosis approaches $\mathcal{K}_r^{\text{st}} \rightarrow 1$, recovering the overdamped passive Brownian result [55] (Fig. 4). In contrast, for strong resetting or large inertia ($Mr \rightarrow \infty$), it saturates to a finite value $\mathcal{K}_r^{\text{st}} \rightarrow 19$. Thus, the product Mr controls the position excess kurtosis $\mathcal{K}_r^{\text{st}}$, which interpolates smoothly between 1 and 19 (Fig. 4(a)).

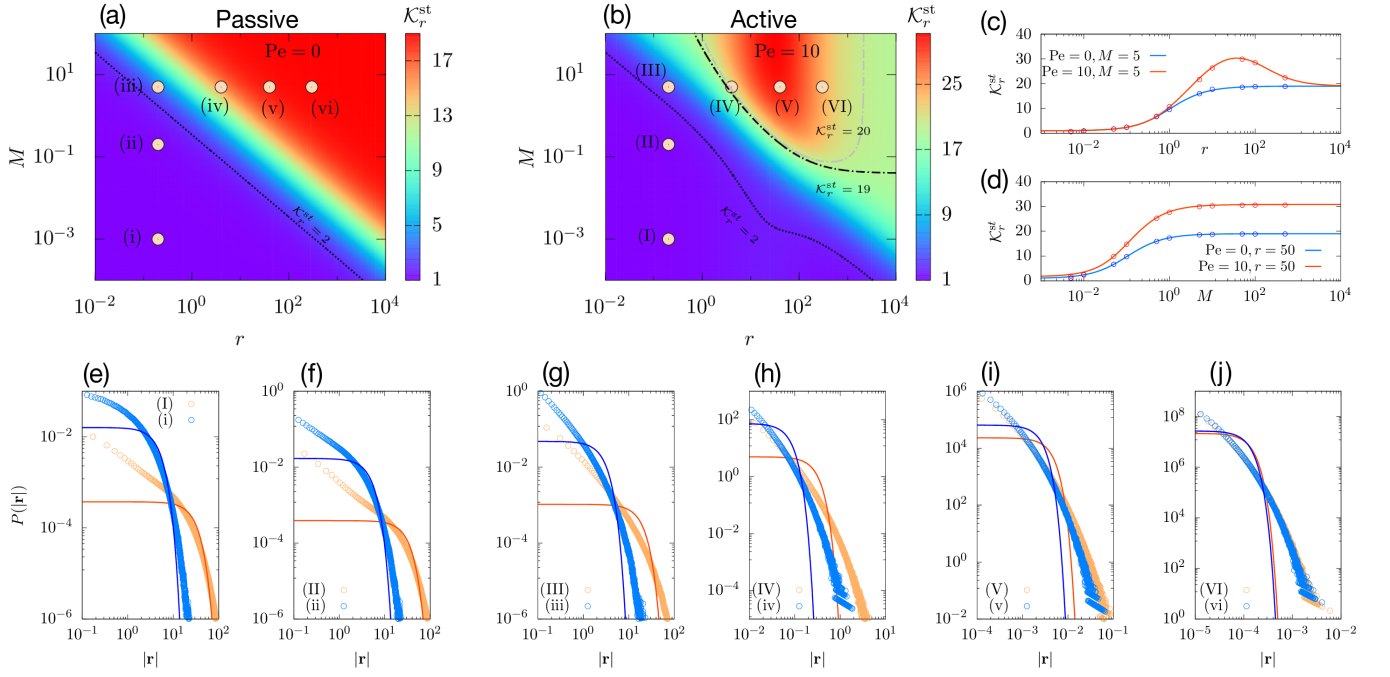


FIG. 4. Phase diagrams using position excess kurtosis as primary metric. Steady-state excess kurtosis of position, $\mathcal{K}_r^{\text{st}}$. Heat maps in the r - M plane for (a) a passive inertial Brownian particle under resetting ($Pe = 0$) and (b) an inertial ABP under resetting. (c,d) Line plots of $\mathcal{K}_r^{\text{st}}$ as a function of (c) reset rate r and (d) inertia M at representative parameter values (lines: theory; symbols: simulations). (e)-(j) Steady-state probability distributions of the displacement magnitude $|\mathbf{r}| = \sqrt{x^2 + y^2}$ at selected points (i)-(vi) in panel (a) and (I)-(VI) in panel (b), illustrating the crossover from weakly non-Gaussian statistics to heavy-tailed, strongly non-Gaussian regimes and the emergence of re-entrant behavior at large inertia and finite activity.

TABLE II. Limiting behavior and asymptotic scaling of the steady-state excess kurtosis of velocity $\mathcal{L}_r^{\text{st}}$ and position $\mathcal{K}_r^{\text{st}}$ for different limits of inertia M and reset rate r . “NO SS”: no steady state. “NA”: undefined in overdamped limit. Scaling refers to asymptotic limits at fixed remaining parameters.

Limit	Velocity excess kurtosis $\mathcal{L}_r^{\text{st}}$	Position excess kurtosis $\mathcal{K}_r^{\text{st}}$
No reset ($r = 0$) [44]	$\mathcal{L}_r^{\text{st}} \leq 0$ (Eq. (11))	NO SS
Overdamped Brownian ($M = 0$, $Pe = 0$) [55]	NA	1
Overdamped ABP ($M = 0$) [55]	NA	$1 \leq \mathcal{K}_r^{\text{st}} < 2$ (Eq. (14))
Underdamped Brownian ($Pe = 0$)	$\frac{Mr}{Mr + 4}$	$1 < \mathcal{K}_r^{\text{st}} < 19$ (Eq. (13))
Our model: Low reset rate	$\mathcal{L}_r^{\text{st}} \leq 0$	$\mathcal{K}_r^{\text{st}} \rightarrow 1$
Our model: High reset rate	$0 < \mathcal{L}_r^{\text{st}} < 1$; increases with M	finite constant; for $Pe = 0$: $\mathcal{K}_r^{\text{st}} \rightarrow 19$
Our model: Low inertia	$\mathcal{L}_r^{\text{st}} \rightarrow 0$	$\mathcal{K}_r^{\text{st}} \rightarrow \mathcal{K}_r^{\text{st}}(M = 0)$
Our model: High inertia	$1 < \mathcal{L}_r^{\text{st}} < 2$; re-entrant in r	finite constant; for $Pe = 0$: $\mathcal{K}_r^{\text{st}} \rightarrow 19$

For any finite activity and in the limit of vanishing inertia ($M \rightarrow 0$), the excess kurtosis reduces to the overdamped ABP under position-orientation stochastic resetting result [55]:

$$\lim_{M \rightarrow 0} \mathcal{K}_r^{\text{st}} = \frac{1}{(4+r)(2+Pe^2+2r)^2 [2Pe^4(2+r) + 4(1+r)^2(4+r) + 4Pe^2(4+r)(1+2r)]}. \quad (14)$$

We analyze Eq. (14) further on the $Pe - r$ plane. For $Pe \rightarrow 0$, one finds $\lim_{Pe \rightarrow 0} \mathcal{K}_r^{\text{st}} \simeq 1$, recovering the

overdamped Brownian particle under stochastic resetting [55]. In contrast, for $Pe \rightarrow \infty$, the limiting value is $\lim_{Pe \rightarrow \infty} \mathcal{K}_r^{\text{st}} \rightarrow 2(2+r)/(4+r)$ which increases monotonically from 1 as $r \rightarrow 0^+$ to 2 as $r \rightarrow \infty$. In the overdamped active regime the position excess kurtosis is bounded within $1 \leq \mathcal{K}_r^{\text{st}} < 2$.

At finite activity and large inertia, the position excess kurtosis exhibits a pronounced re-entrant dependence on the reset rate (Fig. 4(b)). The analytical predictions (Eq. (9); lines) are in excellent agreement with simulations (symbols) (Fig. 4(c,d)), and the corresponding distributions of $|\mathbf{r}|$ explicitly reveal the emergence of heavy-

tailed fluctuations (Fig. 4(e–j)). The limiting behaviors across the different regimes are summarized in Table II.

The expansion of excess kurtosis of position at small reset rate leads to

$$\begin{aligned} \lim_{r \rightarrow 0} \mathcal{K}_r^{\text{st}} &= 1 + c_1(M, \text{Pe})r + \mathcal{O}(r^2), \\ c_1(M, \text{Pe}) &= 3M + \frac{\text{Pe}^4(1 - 3M) + 8\text{Pe}^2(2 + M)}{4(2 + \text{Pe}^2)^2(1 + M)}, \end{aligned} \quad (15)$$

showing that deviations from the overdamped Brownian baseline $\mathcal{K}_r^{\text{st}} = 1$ enter linearly in the reset rate. The coefficient $c_1(M, \text{Pe})$ quantifies the joint influence of inertia and activity. The purely inertial contribution $3M$ is strictly positive, implying that inertia enhances non-Gaussianity in the position statistics by introducing short-time ballistic displacements within each excursion. The activity-dependent correction vanishes as $\mathcal{O}(\text{Pe}^2)$ for $\text{Pe} \ll 1$, recovering the passive limit $\mathcal{K}_r^{\text{st}} = 1 + 3Mr + \mathcal{O}(r^2)$. For finite activity it may either enhance or partially offset the inertial contribution, but the full coefficient remains positive in the explored parameter range, so the excess kurtosis initially increases above unity as the reset rate is increased from very small values. At large reset rate, the position excess kurtosis reads

$$\lim_{r \rightarrow \infty} \mathcal{K}_r^{\text{st}} = 19 + \frac{45}{2} \left(\text{Pe}^2 - \frac{4}{M} \right) \frac{1}{r} + \mathcal{O}(r^{-2}), \quad (16)$$

which shows that in the strong-resetting regime the position excess kurtosis saturates to the universal underdamped-resetting value 19, with a leading correction $\mathcal{O}(1/r)$ whose sign depends on the competition between activity and inertia. In particular, for $\text{Pe}^2 > 4/M$ the kurtosis approaches 19 from above, whereas for $\text{Pe}^2 < 4/M$ it approaches from below. Together, these two asymptotic limits at small and large reset rates explain the emergence of non-monotonic (re-entrant) dependence on the reset rate at sufficiently large inertia and finite activity (Fig. 4(b,c)). The phase diagrams in the $r - \text{Pe}$ and $M - \text{Pe}$ planes reveal a crossover from weakly non-Gaussian behavior at small reset rates or low inertia to strongly non-Gaussian, heavy-tailed regimes at large reset rates and large inertia, with non-monotonic dependence on the reset rate emerging only at sufficiently large activity (Appendix Fig. 6).

V. CONCLUSIONS

We have demonstrated that inertia dramatically alters the steady-state statistics of active particles under stochastic resetting, giving rise to enhanced typical localization, strong non-Gaussian fluctuations, and distinct scaling regimes in both displacement and velocity statistics. Whereas overdamped active particles under resetting in confinement exhibits modest deviations from Gaussianity, the inclusion of inertia produces

qualitatively new behavior: the mean-squared displacement decays as r^{-3} at high reset rates and as M^{-2} at large inertia, and the excess kurtosis exhibits pronounced re-entrant trends reflecting competition between persistence, relaxation, and resetting. These results establish inertia as a key control variable in reset-driven nonequilibrium steady states, bridging the overdamped active matter framework and the largely unexplored inertial regime.

The exact moment framework yields closed-form expressions for steady-state fluctuations up to fourth order, enabling a quantitative characterization of non-Gaussian statistics. Kurtosis-based phase diagrams demonstrate that inertia and resetting produce heavy-tailed velocity and displacement distributions, with a re-entrant dependence that identifies inertial momentum relaxation as a key control parameter for rare fluctuations. These predictions are experimentally accessible in platforms ranging from inertial colloids and optically trapped active particles to programmable robotic agents, where reset protocols can be used to tune localization and rare long excursions (tail weight). More broadly, this work establishes an analytically tractable framework connecting inertia, stochastic resetting, and extreme fluctuations in active systems, with implications for active matter, search processes, and autonomous agents. By showing that inertia can be harnessed to amplify rare events and modulate spatial statistics, our results suggest new strategies for controlling active transport in synthetic and biological systems. Extensions incorporating rotational inertia [49, 57] or external potentials [45] provide a natural route to broaden the framework toward active suspensions, granular systems, and mobile robotics.

Our results show that inertia qualitatively reshapes active dynamics under stochastic resetting, enhancing rare fluctuations and producing strongly non-Gaussian steady states. These predictions are directly testable in robotic and colloidal platforms, where re-entrant kurtosis behavior and distinct scaling regimes at large inertia or reset rates can be probed [58, 59]. Reset protocols further provide a flexible design space through partial, adaptive, or stochastic resetting to tailor exploration strategies and sampling efficiency [22, 26, 28, 60, 61]. First-passage observables quantify the efficiency of locating specific targets [28], whereas steady-state spatial statistics (e.g., MSD and kurtosis) characterize the global structure and the exploration process [39, 55]. These two aspects are related but not equivalent: heavy-tailed steady states can coexist with poor target-finding efficiency when large excursions are rare. In summary, our results present inertial active matter under resetting as a fertile framework to connect active matter, search theory, and autonomous systems, with clear implications for future theory and experiment.

DATA AVAILABILITY

All data supporting the findings of this study are available within the manuscript.

CODE AVAILABILITY

Code supporting this study is available from the corresponding author upon reasonable request.

ACKNOWLEDGEMENTS

We gratefully acknowledge Debasish Chaudhuri and Priyo Shankar Pal for their insightful feedback and discussions. The numerical simulations were performed using SAMKHYA, the High-Performance Computing Facility provided by the Institute of Physics, Bhubaneswar.

-
- [1] P. Romanczuk, M. Bär, W. Ebeling, B. Lindner, and L. Schimansky-Geier, Active brownian particles: From individual to collective stochastic dynamics, *Eur. Phys. J. - Special Topics* **202**, 1 (2012).
- [2] M. C. Marchetti, J. F. Joanny, S. Ramaswamy, T. B. Liverpool, J. Prost, M. Rao, and R. A. Simha, Hydrodynamics of soft active matter, *Rev. Mod. Phys.* **85**, 1143 (2013).
- [3] C. Bechinger, R. Di Leonardo, H. Löwen, C. Reichhardt, G. Volpe, and G. Volpe, Active particles in complex and crowded environments, *Reviews of Modern Physics* **88**, 045006 (2016).
- [4] U. Basu, S. Sabhapandit, and I. Santra, Target search by active particles, in *Target Search Problems*, edited by D. Grebenkov, R. Metzler, and G. Oshanin (Springer, Cham, 2024) pp. 463–487.
- [5] G. M. Viswanathan, M. G. E. da Luz, E. P. Raposo, and H. E. Stanley, *The Physics of Foraging: An Introduction to Random Searches and Biological Encounters* (Cambridge University Press, Cambridge, UK, 2011).
- [6] G. Volpe and G. Volpe, The topography of the environment alters the optimal search strategy for active particles, *Proceedings of the National Academy of Sciences of the United States of America* **114**, 11350 (2017).
- [7] S. Palagi and P. Fischer, Bioinspired microrobots, *Nature Reviews Materials* **3**, 113 (2018).
- [8] M. R. Evans and S. N. Majumdar, Diffusion with stochastic resetting, *Phys. Rev. Lett.* **106**, 160601 (2011).
- [9] M. R. Evans and S. N. Majumdar, Diffusion with optimal resetting, *Journal of Physics A: Mathematical and Theoretical* **44**, 435001 (2011).
- [10] S. Reuveni, M. Urbakh, and J. Klafter, Role of substrate unbinding in michaelis–menten enzymatic reactions, *Proceedings of the National Academy of Sciences of the United States of America* **111**, 4391 (2014).
- [11] T. Rotbart, S. Reuveni, and M. Urbakh, Michaelis-menten reaction scheme as a unified approach towards the optimal restart problem, *Phys. Rev. E* **92**, 060101 (2015).
- [12] E. Roldán, A. Lisica, D. Sánchez-Taltavull, and S. W. Grill, Stochastic resetting in backtrack recovery by rna polymerases, *Phys. Rev. E* **93**, 062411 (2016).
- [13] A. Pal and S. Reuveni, First passage under restart, *Phys. Rev. Lett.* **118**, 030603 (2017).
- [14] T. Robin, S. Reuveni, and M. Urbakh, Single-molecule theory of enzymatic inhibition, *Nature Communications* **9**, 779 (2018).
- [15] P. C. Bressloff, Modeling active cellular transport as a directed search process with stochastic resetting and delays, *Journal of Physics A: Mathematical and Theoretical* **53**, 355001 (2020).
- [16] M. R. Evans, S. N. Majumdar, and G. Schehr, Stochastic resetting and applications, *Journal of Physics A: Mathematical and Theoretical* **53**, 193001 (2020).
- [17] D. Gupta, Stochastic resetting in underdamped brownian motion, *Journal of Statistical Mechanics: Theory and Experiment*, 033212 (2019).
- [18] S. Gupta and A. M. Jayannavar, Stochastic resetting: A (very) brief review, *Frontiers in Physics* **10**, 789097 (2022).
- [19] M. R. Evans and S. N. Majumdar, Run and tumble particle under resetting: a renewal approach, *Journal of Physics A: Mathematical and Theoretical* **51**, 475003 (2018).
- [20] I. Santra, U. Basu, and S. Sabhapandit, Run-and-tumble particles in two dimensions: Marginal position distributions, *Physical Review E* **101**, 62120 (2020).
- [21] P. C. Bressloff, Occupation time of a run-and-tumble particle with resetting, *Phys. Rev. E* **102**, 042135 (2020).
- [22] V. Kumar, O. Sadekar, and U. Basu, Active brownian motion in two dimensions under stochastic resetting, *Phys. Rev. E* **102**, 052129 (2020).
- [23] D. Boyer and S. N. Majumdar, Active particle in one dimension subjected to resetting with memory, *Phys. Rev. E* **109**, 054105 (2024).
- [24] A. Ghosh, S. Mandal, and S. Chaki, Anisotropic active brownian particle in two dimensions under stochastic resetting, *Phys. Rev. E* **113**, 014142 (2026).
- [25] F. Peruani and D. Chaudhuri, Active stop and go motion: A strategy to improve spatial exploration and survival, *Phys. Rev. E* **112**, L033402 (2025).
- [26] Y. Baouche, T. Franosch, M. Meiners, and C. Kurzthaler, Active brownian particle under stochastic orientational resetting, *New Journal of Physics* **26**, 073041 (2024).
- [27] P. S. Pal, J.-M. Park, A. Pal, H. Park, and J. S. Lee, Active motion can be beneficial for target search with resetting in a thermal environment, *Phys. Rev. E* **110**, 054124 (2024).
- [28] Y. Baouche and C. Kurzthaler, Optimal first-passage times of active brownian particles under stochastic resetting, *Soft Matter* **21**, 5998 (2025).
- [29] N. Koumakis, A. Gnoli, C. Maggi, A. Puglisi, and R. Di Leonardo, Mechanism of self-propulsion in 3d-printed active granular particles, *New Journal of Physics* **18**, 113046 (2016).

- [30] C. Scholz, S. Jahanshahi, A. Ldov, and H. Löwen, Inertial delay of self-propelled particles, *Nature Communications* **9**, 5156 (2018).
- [31] A. Deblais, T. Barois, T. Guerin, P. H. Delville, R. Vaudaine, J. S. Lintuvuori, J. F. Boudet, J. C. Baret, and H. Kellay, Boundaries control collective dynamics of inertial self-propelled robots, *Phys. Rev. Lett.* **120**, 188002 (2018).
- [32] T. Dombrowski, S. K. Jones, G. Katsikis, A. P. S. Bhalla, B. E. Griffith, and D. Klotsa, Transition in swimming direction in a model self-propelled inertial swimmer, *Phys. Rev. Fluids* **4**, 021101 (2019).
- [33] O. Dauchot and V. Démery, Dynamics of a self-propelled particle in a harmonic trap, *Phys. Rev. Lett.* **122**, 068002 (2019).
- [34] H. Löwen, Inertial effects of self-propelled particles: From active brownian to active langevin motion, *The Journal of Chemical Physics* **152**, 040901 (2020).
- [35] M. Sandoval, Pressure and diffusion of active matter with inertia, *Phys. Rev. E* **101**, 012606 (2020).
- [36] G. H. P. Nguyen, R. Wittmann, and H. Löwen, Active ornstein–uhlenbeck model for self-propelled particles with inertia, *Journal of Physics: Condensed Matter* **34**, 035101 (2022).
- [37] A. Altshuler, O. L. Bonomo, N. Gorohovsky, S. Marchini, E. Rosen, O. Tal-Friedman, S. Reuveni, and Y. Roichman, Environmental memory facilitates search with home returns, *Phys. Rev. Res.* **6**, 023255 (2024).
- [38] S. Paramanick, A. Biswas, H. Soni, A. Pal, and N. Kumar, Uncovering universal characteristics of homing paths using foraging robots, *PRX Life* **2**, 033007 (2024).
- [39] K. S. Olsen, H. Löwen, and L. Caprini, Optimal area exploration by resetting active particles, arXiv preprint arXiv:2510.01087 10.48550/arXiv.2510.01087 (2025), arXiv:2510.01087 [cond-mat.soft].
- [40] A. Sinha, S. Jangid, T. Sadhu, and S. Ghosh, Optimal navigation in a noisy environment (2025), arXiv:2512.20336 [cond-mat.stat-mech].
- [41] L. L. Gutierrez-Martinez and M. Sandoval, Inertial effects on trapped active matter, *The Journal of Chemical Physics* **153**, 044906 (2020).
- [42] L. Caprini and U. Marini Bettolo Marconi, Inertial self-propelled particles, *The Journal of Chemical Physics* **154**, 024902 (2021).
- [43] J. Mayer Martins and R. Wittkowski, Inertial dynamics of an active brownian particle, *Phys. Rev. E* **106**, 034616 (2022).
- [44] M. Patel and D. Chaudhuri, Exact moments and re-entrant transitions in the inertial dynamics of active brownian particles, *New Journal of Physics* **25**, 123048 (2023).
- [45] M. Patel and D. Chaudhuri, Exact moments for trapped active particles: inertial impact on steady-state properties and re-entrance, *New Journal of Physics* **26**, 073048 (2024).
- [46] M. Patel, S. Paul, and D. Chaudhuri, Crossover dynamics and non-gaussian fluctuations in inertial active chains (2025), arXiv:2511.13270 [cond-mat.stat-mech].
- [47] E. A. Lisin and I. I. Lisina, Active brownian motion with inertia: The role of dimensionality, *Physics of Fluids* **37**, 021709 (2025).
- [48] J. Palacci, S. Sacanna, A. P. Steinberg, D. J. Pine, and P. M. Chaikin, Living crystals of light-activated colloidal surfers, *Science* **339**, 936 (2013).
- [49] L. Caprini, R. K. Gupta, and H. Löwen, Role of rotational inertia for collective phenomena in active matter, *Physical Chemistry Chemical Physics* **24**, 24910 (2022).
- [50] E. A. Lisin and I. I. Lisina, Fully inertial active brownian particle in a harmonic potential, *Phys. Rev. E* **113**, 015417 (2026).
- [51] J. J. Hermans and R. Ullman, The statistics of stiff chains, with applications to light scattering, *Physica* **18**, 951 (1952).
- [52] A. Shee, A. Dhar, and D. Chaudhuri, Active brownian particles: mapping to equilibrium polymers and exact computation of moments, *Soft Matter* **16**, 4776 (2020).
- [53] D. Chaudhuri and A. Dhar, Active brownian particle in harmonic trap: exact computation of moments, and re-entrant transition, *Journal of Statistical Mechanics: Theory and Experiment* **2021**, 013207 (2021).
- [54] A. Pattanayak, A. Shee, D. Chaudhuri, and A. Chaudhuri, Impact of torque on active brownian particle: exact moments in two and three dimensions, *New Journal of Physics* **26**, 083024 (2024).
- [55] A. Shee, Active brownian particle under stochastic position and orientation resetting in a harmonic trap, *Journal of Physics Communications* **9**, 025003 (2025).
- [56] G. E. Uhlenbeck and L. S. Ornstein, On the theory of the brownian motion, *Physical Review* **36**, 823 (1930).
- [57] E. A. Lisin, O. S. Vaulina, I. I. Lisina, and O. F. Petrov, Motion of a self-propelled particle with rotational inertia, *Physical Chemistry Chemical Physics* **24**, 14150 (2022).
- [58] O. Tal-Friedman, A. Pal, A. Sekhon, S. Reuveni, and Y. Roichman, Experimental realization of diffusion with stochastic resetting, *The Journal of Physical Chemistry Letters* **11**, 7350–7355 (2020).
- [59] F. Faisant, B. Besga, A. Petrosyan, S. Ciliberto, and S. N. Majumdar, Optimal mean first-passage time of a brownian searcher with resetting in one and two dimensions: experiments, theory and numerical tests, *Journal of Statistical Mechanics: Theory and Experiment* , 113203 (2021).
- [60] K. S. Olsen and H. Löwen, Dynamics of inertial particles under velocity resetting, *Journal of Statistical Mechanics: Theory and Experiment* , 033210 (2024).
- [61] T. D. Keidar, O. Blumer, B. Hirshberg, and S. Reuveni, Adaptive resetting for informed search strategies and the design of non-equilibrium steady-states, *Nature Communications* **16**, 7259 (2025).

Appendix A: Mapping to overdamped ABP in a harmonic trap

It is instructive to note that the dimensionless velocity dynamics of a free inertial ABP (Eq. (2) in main text)

$$M d\mathbf{v} = -\mathbf{v} dt + \text{Pe} \hat{\mathbf{u}} dt + \sqrt{2} d\mathbf{B}^t, \quad (\text{A1})$$

can be mapped exactly onto the position dynamics of an overdamped ABP in a harmonic potential of stiffness β [53],

$$d\mathbf{r} = -\beta \mathbf{r} dt + v_a \hat{\mathbf{u}} dt + \sqrt{2} d\mathbf{B}^t. \quad (\text{A2})$$

Identifying coefficients yields the correspondence

$$\beta = \frac{1}{M}, \quad v_a = \frac{\text{Pe}}{M}, \quad (\text{A3})$$

along with effective noise strength mapping $2/M^2 \rightarrow 2$, so that the inertial velocity process is mathematically equivalent to the position of an overdamped ABP confined in a harmonic trap with parameters (β, v_a) .

Under stochastic resetting, this mapping implies that the velocity statistics of an inertial particle mirror those of a harmonically trapped overdamped ABP with the above parameter substitution [55]. By contrast, the *position* of an inertial ABP under resetting does not follow this simple mapping, as it couples to velocity and therefore exhibits rich complex behavior.

Appendix B: Moments generator framework

The probability distribution $P(\mathbf{r}, \mathbf{v}, \hat{\mathbf{u}}, t)$ of the position \mathbf{r} , the velocity \mathbf{v} and the heading (or orientation) $\hat{\mathbf{u}}$ of the particle follows the Fokker-Planck equation [44, 51]

$$\begin{aligned} \partial_t P &= -\nabla \cdot (\mathbf{v} P) - (1/M) \nabla_v \cdot ((\text{Pe} \hat{\mathbf{u}} - \mathbf{v}) P) \\ &\quad + (1/M^2) \nabla_v^2 P + \nabla_u^2 P, \end{aligned} \quad (\text{B1})$$

where ∇ , ∇_v , and ∇_u is the gradient on the position, velocity, and orientation space, respectively.

Utilizing the Laplace transform $\tilde{P}(\mathbf{r}, \mathbf{v}, \hat{\mathbf{u}}, s) = \int_0^\infty dt e^{-st} P(\mathbf{r}, \mathbf{v}, \hat{\mathbf{u}}, t)$ and defining the mean of an observable $\langle \psi \rangle_s = \int d\mathbf{r} d\mathbf{v} d\hat{\mathbf{u}} \psi(\mathbf{r}, \mathbf{v}, \hat{\mathbf{u}}) \tilde{P}(\mathbf{r}, \mathbf{v}, \hat{\mathbf{u}}, s)$, multiplying by $\psi(\mathbf{r}, \mathbf{v}, \hat{\mathbf{u}})$ and integrating over all possible $(\mathbf{r}, \mathbf{v}, \hat{\mathbf{u}})$, we find,

$$\begin{aligned} -\langle \psi \rangle_0 + s \langle \psi \rangle_s &= \langle \mathbf{v} \cdot \nabla \psi \rangle_s + (\text{Pe}/M) \langle \hat{\mathbf{u}} \cdot \nabla_v \psi \rangle_s \\ &\quad - (1/M) \langle \mathbf{v} \cdot \nabla_v \psi \rangle_s + (1/M^2) \langle \nabla_v^2 \psi \rangle_s \\ &\quad + \langle \nabla_u^2 \psi \rangle_s, \end{aligned} \quad (\text{B2})$$

where the initial condition sets $\langle \psi \rangle_0 = \int d\mathbf{r} d\mathbf{v} d\hat{\mathbf{u}} \psi(\mathbf{r}, \mathbf{v}, \hat{\mathbf{u}}) P(\mathbf{r}, \mathbf{v}, \hat{\mathbf{u}}, 0)$. Without any loss of generality, we consider the initial condition to follow $P(\mathbf{r}, \hat{\mathbf{u}}, 0) = \delta(\mathbf{r} - \mathbf{r}_0) \delta(\mathbf{v} - \mathbf{v}_0) \delta(\hat{\mathbf{u}} - \hat{\mathbf{u}}_0)$, where \mathbf{r}_0 , \mathbf{v}_0 , and $\hat{\mathbf{u}}_0$ are the initial position, velocity, and orientation respectively. Equation (B2) can be utilize to compute exact moments as a function of time without stochastic resetting; see Patel *et al* [44].

Under stochastic resetting of both position and orientation, the moments satisfy the renewal equation [22, 55]

$$\langle \psi(t) \rangle_r = e^{-rt} \langle \psi(t) \rangle + r \int_0^t dt' e^{-rt'} \langle \psi(t') \rangle. \quad (\text{B3})$$

This formalism allows us to compute exact expressions for moments up to fourth order and to analyze their long-time limit ($t \rightarrow \infty$), which defines the non-equilibrium steady state. Alternatively, the steady state under stochastic resetting can be obtained directly from the Final Value Theorem (FVT) applied to Eq. (B2)

$$\langle \psi \rangle_r^{\text{st}} = r \langle \psi \rangle_s (s = r). \quad (\text{B4})$$

We present the primary results in the main text and provide full derivations below.

Appendix C: Derivation of second order moments

Orientation: Without stochastic resetting, the Laplace space orientation $\langle \hat{\mathbf{u}} \rangle_s$ can be obtain from Eq. (B2) using $\langle \nabla_u^2 \hat{\mathbf{u}} \rangle = -\hat{\mathbf{u}}$, while $\mathbf{v} \cdot \nabla(\hat{\mathbf{u}}) = \hat{\mathbf{u}} \cdot \nabla_v(\hat{\mathbf{u}}) = \mathbf{v} \cdot \nabla_v(\hat{\mathbf{u}}) = \nabla_v^2(\hat{\mathbf{u}}) = 0$ as

$$\langle \hat{\mathbf{u}} \rangle_s = \frac{\hat{\mathbf{u}}_0}{s+1}. \quad (\text{C1})$$

The Laplace transformation of above equation gives the full dynamics in absence of stochastic resetting as $\langle \hat{\mathbf{u}} \rangle(t) = \hat{\mathbf{u}}_0 e^{-t}$. The full orientation evolution under stochastic resetting can be obtained by using $\langle \hat{\mathbf{u}} \rangle(t)$ in Eq. (B3). One can directly obtain the steady state orientation under stochastic resetting using Eq. (B4) as

$$\langle \hat{\mathbf{u}} \rangle_r^{\text{st}} = \frac{r \hat{\mathbf{u}}_0}{r+1}. \quad (\text{C2})$$

Second moment of Velocity: We set $\psi = \mathbf{v}^2$ in Eq. (B2) and use $\langle \psi \rangle_0 = \mathbf{v}_0^2$, $\mathbf{v} \cdot \nabla(\mathbf{v}^2) = 0$, $\langle \mathbf{v} \cdot \nabla_v(\mathbf{v}^2) \rangle_s = 2 \langle \mathbf{v}^2 \rangle_s$, $\langle \hat{\mathbf{u}} \cdot \nabla_v(\mathbf{v}^2) \rangle_s = 2 \langle \hat{\mathbf{u}} \cdot \mathbf{v} \rangle_s$, $\nabla_v^2(\mathbf{v}^2) = 4/s$ and $\nabla_u^2(\mathbf{v}^2) = 0$ to obtain moments in absence of resetting as

$$\langle \mathbf{v}^2 \rangle_s = \frac{1}{s+2/M} \left(\mathbf{v}_0^2 + \frac{2\text{Pe} \langle \hat{\mathbf{u}} \cdot \mathbf{v} \rangle_s}{M} + \frac{4}{sM^2} \right). \quad (\text{C3})$$

We again set $\psi = \hat{\mathbf{u}} \cdot \mathbf{v}$ in Eq. (B2) to get $\langle \hat{\mathbf{u}} \cdot \mathbf{v} \rangle_s = [\hat{\mathbf{u}}_0 \cdot \mathbf{v}_0 + \text{Pe}/(sM)]/[s+1+1/M]$. Following Eq. (B4), we use $\langle \mathbf{v}^2 \rangle_s$ and $\langle \hat{\mathbf{u}} \cdot \mathbf{v} \rangle_s$ to get the steady state second moment of velocity under stochastic resetting as Eq. (5) in the main text, where we have used the initial condition as $\mathbf{r}_0 = \mathbf{0}$ and $\mathbf{v}_0 = \mathbf{0}$.

Second moment of Displacement: We follow the same step as for velocity dynamics to get the second moment of displacement in absence of stochastic resetting using Eq. (B2) as $s \langle \mathbf{r}^2 \rangle_s = \langle \mathbf{r}^2 \rangle_0 + 2 \langle \mathbf{v} \cdot \mathbf{r} \rangle_s$. We further use $\psi = \mathbf{v} \cdot \mathbf{r}$ and $\psi = \hat{\mathbf{u}} \cdot \mathbf{r}$ in Eq. (B2) to get $(s+1/M) \langle \mathbf{v} \cdot \mathbf{r} \rangle_s = \langle \mathbf{v} \cdot \mathbf{r} \rangle_0 + \langle \mathbf{v}^2 \rangle_s + \text{Pe} \langle \hat{\mathbf{u}} \cdot \mathbf{r} \rangle_s / M$ and $(s+1) \langle \hat{\mathbf{u}} \cdot \mathbf{r} \rangle_s = \langle \hat{\mathbf{u}} \cdot \mathbf{r} \rangle_0 + \langle \hat{\mathbf{u}} \cdot \mathbf{v} \rangle_s$, respectively. We use these moments in Eq. (B4) to get the steady state mean squared displacement under stochastic resetting for initial condition $\mathbf{r}_0 = \mathbf{0}$, $\mathbf{v}_0 = \mathbf{0}$ as Eq. (7) presented in main text.

Gaussian from second order moments: Given the exact steady-state second moments derived above, we write the corresponding Gaussian. Writing the variances as

$$\sigma_r^2 \equiv \frac{1}{2} \langle \mathbf{r}^2 \rangle_r^{\text{st}}, \quad \sigma_v^2 \equiv \frac{1}{2} \langle \mathbf{v}^2 \rangle_r^{\text{st}}, \quad (\text{C4})$$

the Gaussian distributions of position and velocity reads

$$\mathcal{P}_G(|\mathbf{r}|) = \frac{1}{2\pi\sigma_r^2} \exp\left(-\frac{|\mathbf{r}|^2}{2\sigma_r^2}\right), \quad (\text{C5})$$

$$\mathcal{P}_G(|\mathbf{v}|) = \frac{1}{2\pi\sigma_v^2} \exp\left(-\frac{|\mathbf{v}|^2}{2\sigma_v^2}\right). \quad (\text{C6})$$

We use this Gaussian distribution as a reference to visually quantify deviations of the numerically computed distributions.

Appendix D: Derivation of fourth order moments

We set $\psi = \mathbf{v}^4$ and $\psi = \mathbf{r}^4$ in Eq. (B2), respectively, to obtain the fourth moments of the velocity and displacement vectors, in the absence of stochastic resetting, in Laplace space:

$$(s + 4/M)\langle \mathbf{v}^4 \rangle_s = \mathbf{v}_0^4 + \frac{4\text{Pe}}{M}\langle (\hat{\mathbf{u}} \cdot \mathbf{v})\mathbf{v}^2 \rangle_s + \frac{16}{M^2}\langle \mathbf{v}^2 \rangle_s, \quad (\text{D1})$$

$$(s + 3/M + 1)\langle (\hat{\mathbf{u}} \cdot \mathbf{v})\mathbf{v}^2 \rangle_s = (\hat{\mathbf{u}}_0 \cdot \mathbf{v}_0)\mathbf{v}_0^2 + \frac{\text{Pe}}{M}\langle \mathbf{v}^2 \rangle_s + \frac{2\text{Pe}}{M}\langle (\hat{\mathbf{u}} \cdot \mathbf{v}) \rangle_s + \frac{8}{M^2}\langle \hat{\mathbf{u}} \cdot \mathbf{v} \rangle_s, \quad (\text{D2})$$

$$(s + 2/M + 4)\langle (\hat{\mathbf{u}} \cdot \mathbf{v})^2 \rangle_s = (\hat{\mathbf{u}}_0 \cdot \mathbf{v}_0)^2 + \frac{2\text{Pe}}{M}\langle \hat{\mathbf{u}} \cdot \mathbf{v} \rangle_s + \frac{2}{sM^2} + 2\langle \mathbf{v}^2 \rangle_s, \quad (\text{D3})$$

$$s\langle \mathbf{r}^4 \rangle_s = 4\langle (\mathbf{v} \cdot \mathbf{r})\mathbf{r}^2 \rangle_s, \quad (\text{D4})$$

$$(s + 1/M)\langle (\mathbf{v} \cdot \mathbf{r})\mathbf{r}^2 \rangle_s = \langle (\mathbf{v}_0 \cdot \mathbf{r}_0)\mathbf{r}_0^2 + \langle \mathbf{v}^2\mathbf{r}^2 \rangle_s + 2\langle (\mathbf{v} \cdot \mathbf{r}) \rangle_s + \frac{\text{Pe}}{M}\langle (\hat{\mathbf{u}} \cdot \mathbf{r})\mathbf{r}^2 \rangle_s, \quad (\text{D5})$$

$$(s + 2/M)\langle \mathbf{v}^2\mathbf{r}^2 \rangle_s = \mathbf{v}_0^2\mathbf{r}_0^2 + 2\langle (\mathbf{v} \cdot \mathbf{r})\mathbf{v}^2 \rangle_s + \frac{2\text{Pe}}{M}\langle (\hat{\mathbf{u}} \cdot \mathbf{v})\mathbf{r}^2 \rangle_s + \frac{4}{M^2}\langle \mathbf{r}^2 \rangle_s, \quad (\text{D6})$$

$$(s + 3/M)\langle (\mathbf{v} \cdot \mathbf{r})\mathbf{v}^2 \rangle_s = (\mathbf{v}_0 \cdot \mathbf{r}_0)\mathbf{v}_0^2 + \langle \mathbf{v}^4 \rangle_s + \frac{\text{Pe}}{M}\langle (\hat{\mathbf{u}} \cdot \mathbf{r})\mathbf{v}^2 \rangle_s + \frac{2\text{Pe}}{M}\langle (\hat{\mathbf{u}} \cdot \mathbf{v})(\mathbf{v} \cdot \mathbf{r}) \rangle_s + \frac{8}{M^2}\langle \mathbf{v} \cdot \mathbf{r} \rangle_s, \quad (\text{D7})$$

$$(s + 2/M + 1)\langle (\hat{\mathbf{u}} \cdot \mathbf{v})(\mathbf{v} \cdot \mathbf{r}) \rangle_s = (\hat{\mathbf{u}}_0 \cdot \mathbf{v}_0)(\mathbf{v}_0 \cdot \mathbf{r}_0) + \langle (\hat{\mathbf{u}} \cdot \mathbf{v})\mathbf{v}^2 \rangle_s + \frac{\text{Pe}}{M}\langle \mathbf{v} \cdot \mathbf{r} \rangle_s + \frac{\text{Pe}}{M}\langle (\hat{\mathbf{u}} \cdot \mathbf{v})(\hat{\mathbf{u}} \cdot \mathbf{r}) \rangle_s + \frac{2}{M^2}\langle \hat{\mathbf{u}} \cdot \mathbf{r} \rangle_s, \quad (\text{D8})$$

$$(s + 2/M + 1)\langle (\hat{\mathbf{u}} \cdot \mathbf{r})\mathbf{v}^2 \rangle_s = (\hat{\mathbf{u}}_0 \cdot \mathbf{r}_0)\mathbf{v}_0^2 + \langle (\hat{\mathbf{u}} \cdot \mathbf{v})\mathbf{v}^2 \rangle_s + \frac{2\text{Pe}}{M}\langle (\hat{\mathbf{u}} \cdot \mathbf{v})(\hat{\mathbf{u}} \cdot \mathbf{r}) \rangle_s + \frac{4}{M^2}\langle \hat{\mathbf{u}} \cdot \mathbf{r} \rangle_s, \quad (\text{D8})$$

$$(s + 1/M + 4)\langle (\hat{\mathbf{u}} \cdot \mathbf{v})(\hat{\mathbf{u}} \cdot \mathbf{r}) \rangle_s = (\hat{\mathbf{u}}_0 \cdot \mathbf{v}_0)(\hat{\mathbf{u}}_0 \cdot \mathbf{r}_0) + \langle (\hat{\mathbf{u}} \cdot \mathbf{v})^2 \rangle_s + \frac{\text{Pe}}{M}\langle \hat{\mathbf{u}} \cdot \mathbf{r} \rangle_s + 2\langle \mathbf{v} \cdot \mathbf{r} \rangle_s, \quad (\text{D9})$$

$$(s + 1/M + 1)\langle (\hat{\mathbf{u}} \cdot \mathbf{v})\mathbf{r}^2 \rangle_s = (\hat{\mathbf{u}}_0 \cdot \mathbf{v}_0)\mathbf{r}_0^2 + 2\langle (\hat{\mathbf{u}} \cdot \mathbf{v})(\mathbf{v} \cdot \mathbf{r}) \rangle_s + \frac{\text{Pe}}{M}\langle \mathbf{r}^2 \rangle_s, \quad (\text{D10})$$

$$(s + 2/M)\langle (\mathbf{v} \cdot \mathbf{r})^2 \rangle_s = (\mathbf{v}_0 \cdot \mathbf{r}_0)^2 + 2\langle (\mathbf{v} \cdot \mathbf{r})\mathbf{v}^2 \rangle_s + \frac{2\text{Pe}}{M}\langle (\hat{\mathbf{u}} \cdot \mathbf{r})(\mathbf{v} \cdot \mathbf{r}) \rangle_s + \frac{2}{M^2}\langle \mathbf{r}^2 \rangle_s, \quad (\text{D11})$$

$$(s + 1)\langle (\hat{\mathbf{u}} \cdot \mathbf{r})\mathbf{r}^2 \rangle_s = (\hat{\mathbf{u}}_0 \cdot \mathbf{r}_0)\mathbf{r}_0^2 + \langle (\hat{\mathbf{u}} \cdot \mathbf{v})\mathbf{r}^2 \rangle_s + 2\langle (\hat{\mathbf{u}} \cdot \mathbf{r})(\mathbf{v} \cdot \mathbf{r}) \rangle_s, \quad (\text{D12})$$

$$(s + 1/M + 1)\langle (\hat{\mathbf{u}} \cdot \mathbf{r})(\mathbf{v} \cdot \mathbf{r}) \rangle_s = (\hat{\mathbf{u}}_0 \cdot \mathbf{r}_0)(\mathbf{v}_0 \cdot \mathbf{r}_0) + \langle (\hat{\mathbf{u}} \cdot \mathbf{v})(\mathbf{v} \cdot \mathbf{r}) \rangle_s + \langle (\hat{\mathbf{u}} \cdot \mathbf{r})\mathbf{v}^2 \rangle_s + \frac{\text{Pe}}{M}\langle (\hat{\mathbf{u}} \cdot \mathbf{r})^2 \rangle_s, \quad (\text{D13})$$

$$(s + 4)\langle (\hat{\mathbf{u}} \cdot \mathbf{r})^2 \rangle_s = (\hat{\mathbf{u}}_0 \cdot \mathbf{r}_0)^2 + 2\langle (\hat{\mathbf{u}} \cdot \mathbf{v})(\hat{\mathbf{u}} \cdot \mathbf{r}) \rangle_s + 2\langle \mathbf{r}^2 \rangle_s. \quad (\text{D14})$$

The inverse Laplace transformation of $\langle \mathbf{v}^4 \rangle_s$ and $\langle \mathbf{r}^4 \rangle_s$ leads to the full time evolution of the fourth moments, $\langle \mathbf{v}^4 \rangle(t)$ and $\langle \mathbf{r}^4 \rangle(t)$, respectively. These results correspond to inertial active Brownian particles in the absence of stochastic resetting and were discussed in detail by Patel *et al.* [44]. We may use Eq. (B3) to obtain exact expressions for the fourth moments, $\langle \mathbf{v}^4 \rangle_r(t)$ and $\langle \mathbf{r}^4 \rangle_r(t)$, in the presence of full stochastic resetting. Since our primary focus in this article is the steady state, we directly employ the Final Value Theorem in Eq. (B4), which leads to

$$\langle \mathbf{v}^4 \rangle_r^{\text{st}} = \frac{\mathcal{A}_1}{\mathcal{B}_1}, \quad (\text{D15})$$

where

$$\begin{aligned} \mathcal{A}_1 &= 64M^3r^3 \\ &+ (96M^3\text{Pe}^2 + 384M^3 + 384M^2)r^2 \\ &+ (24M^3\text{Pe}^4 + 448M^3\text{Pe}^2 + 576M^3 + 384M^2\text{Pe}^2 + 1536M^2 + 704M)r \\ &+ (64M^3\text{Pe}^4 + 256M^3\text{Pe}^2 + 256M^3 + 48M^2\text{Pe}^4 + 896M^2\text{Pe}^2 + 1152M^2 + 384M\text{Pe}^2 + 1280M + 384), \\ \mathcal{B}_1 &= M^2(Mr + 2)(Mr + 4)(Mr + M + 1)(Mr + M + 3)(Mr + 4M + 2). \end{aligned}$$

The above steady state fourth moment of velocity agrees well with numerical simulation, as shown in Fig. 5(a,b). For zero reset rate $r = 0$, $\langle \mathbf{v}^4 \rangle_r^{\text{st}}$ goes as $\sim 8/M^2$ in small inertia limit and $\sim (8 + 8\text{Pe}^2 + 2\text{Pe}^4)/M^2$ in the large inertia limit, as shown in Fig. 5(a). At any finite reset rate $r \neq 0$, $\langle \mathbf{v}^4 \rangle_r^{\text{st}}$ show same scaling of $\sim 8/M^2$ at small inertia. However, at large inertia the behavior is $\sim 8[8(1+r)^2(4+r) + 4(4+r)(2+3r)\text{Pe}^2 + (8+3r)\text{Pe}^4]/[r^2(1+r)^2(4+r)M^4]$, as shown in Fig. 5(a). At any fix inertia, $\langle \mathbf{v}^4 \rangle_r^{\text{st}}$ starts from a fixed value at small reset rate, which is governed by inertia. With increase in reset rate $\langle \mathbf{v}^4 \rangle_r^{\text{st}}$ decreases and goes as $\sim 64/(M^4r^2)$ at large reset rate, as shown in Fig. 5(b).

Again using the Eq. (B4), we can get the steady state fourth moment of position as

$$\langle \mathbf{r}^4 \rangle_r^{\text{st}} = \frac{256(12 + 5rM(5 + 2rM))}{r^2(1 + rM)^2(2 + rM)^2(3 + rM)(4 + rM)} + \frac{\mathcal{A}_2}{\mathcal{B}_2} \text{Pe}^2 + \frac{\mathcal{A}_3}{\mathcal{B}_2(4 + r)(1 + M(4 + r))(2 + M(4 + r))} \text{Pe}^4, \quad (\text{D16})$$

with

$$\begin{aligned} \mathcal{B}_2 &= r^2(1 + r)^2(1 + rM)^2(2 + rM)^2(3 + rM)(4 + rM)(1 + M + rM)^2(2 + M + rM)(3 + M + rM), \\ \mathcal{A}_2 &= (105M^6r^7 + 14M^5(29M + 65)r^6 + 7M^4(M(93M + 431) + 443)r^5 + 5M^3(M(M(108M + 805) + 1725) + 1064)r^4 \\ &\quad + 10M^2(M(M(M(23M + 267) + 926) + 1198) + 486)r^3 + M(M(M(M(5M(8M + 171) + 4628) + 9773) + 8372) \\ &\quad + 2268)r^2 + 4(M + 1)(M(M(M(25M + 219) + 602) + 570) + 108)r + 48(M + 1)^2(M + 2)(M + 3)) , \\ \mathcal{A}_3 &= 8(315M^8r^9 + 693M^7(6M + 5)r^8 + 63M^6(M(349M + 653) + 255)r^7 + M^5(2M(M(29512M + 96487) + 84558) \\ &\quad + 41055)r^6 + 4M^2(M(M(M(M(7328M^2 + 88388M + 334233) + 520114) + 352254) + 99437) + 8976)r^3 \\ &\quad + M^4(M(M(85856M^2 + 449710M + 689867) + 376869) + 63420)r^5 + 2M^3(M(M(M(34584M^2 + 274438 \\ &\quad M + 678807) + 651656) + 248685) + 30480)r^4 + 8M(M(M(M(M(8M(16M(5M + 109) + 10081) + 193597) + \\ &\quad 214555) + 109643) + 23467) + 1494)r^2 + 32(M + 1)(M(M(M(4M(M(100M + 933) + 2935) + 15153) + 7750) \\ &\quad + 1419) + 54)r + 768(M + 1)^2(M + 2)(M + 3)(2M + 1)(4M + 1)) . \end{aligned}$$

The above expression for steady state fourth moment of position agrees well with numerical simulation results, as shown in Fig. 5(c,d). At any finite reset rate, $\langle \mathbf{r}^4 \rangle_r^{\text{st}}$ starts from a saturation value $8[8(1 + r)^2(4 + r) + 4(4 + r)(2 + 3r)\text{Pe}^2 + (8 + 3r)\text{Pe}^4]/[r^2(1 + r)^2(4 + r)]$ at small inertia and decreases with increase in inertia. It vanishes in large limit of inertia as $\sim 1/M^4$, as shown in Fig. 5(c). In the limit of vanishing inertia $M = 0$, $\langle \mathbf{r}^4 \rangle_r^{\text{st}}$ behaves as $\sim 16(2 + \text{Pe}^2)^2/r^2$ at small reset rate and decrease with increase in reset rate. It vanishes as $\sim 64/r^2$ at large reset rate, as shown in Fig. 5(d). For any finite inertia, the small-reset-rate behavior of $\langle \mathbf{r}^4 \rangle_r^{\text{st}}$ is same as in overdamped case. In contrast, in the large-reset-rate limit, $\langle \mathbf{r}^4 \rangle_r^{\text{st}}$ vanishes as $\sim 2560/(M^4r^6)$, as shown in Fig. 5(d).

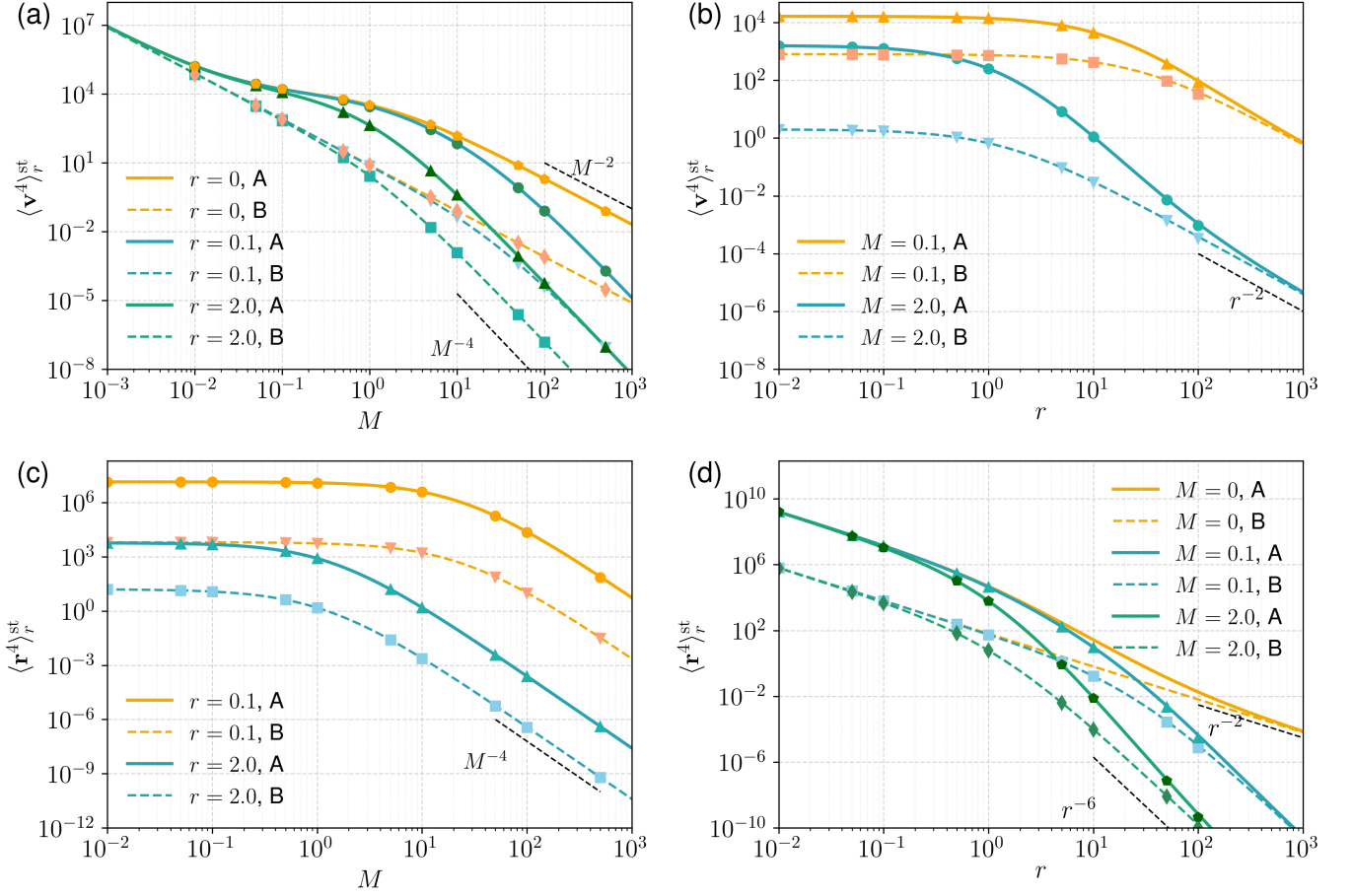


FIG. 5. Steady-state fourth moment of velocity $\langle \mathbf{v}^4 \rangle_r^{\text{st}}$ ((a)–(b)) and position $\langle \mathbf{r}^4 \rangle_r^{\text{st}}$ ((c)–(d)) of inertial active Brownian particles under complete stochastic resetting, comparing active particles ($\text{Pe} = 10$, solid lines, labeled “A”) with passive Brownian particles ($\text{Pe} = 0$, dashed lines, labeled “B”). (a) Fourth moment of velocity as a function of inertia M for reset rates $r = 0, 0.1, 2.0$. (b) Fourth moment of velocity as a function of reset rate r for $M = 0.1, 2.0$. (c) Fourth moment of position as a function of inertia M for reset rates $r = 0.1, 2.0$. (d) Fourth moment of position as a function of reset rate r for $M = 0$ (overdamped), 0.1, and 2.0. Dashed black lines indicate analytic scaling regimes (M^{-2} , M^{-4} , r^{-2} , r^{-6}) in the large- M or large- r limits. These results highlight how inertia and resetting jointly suppress fluctuations, with activity strongly enhancing both fourth moment of position and velocity compared to the Brownian baseline.

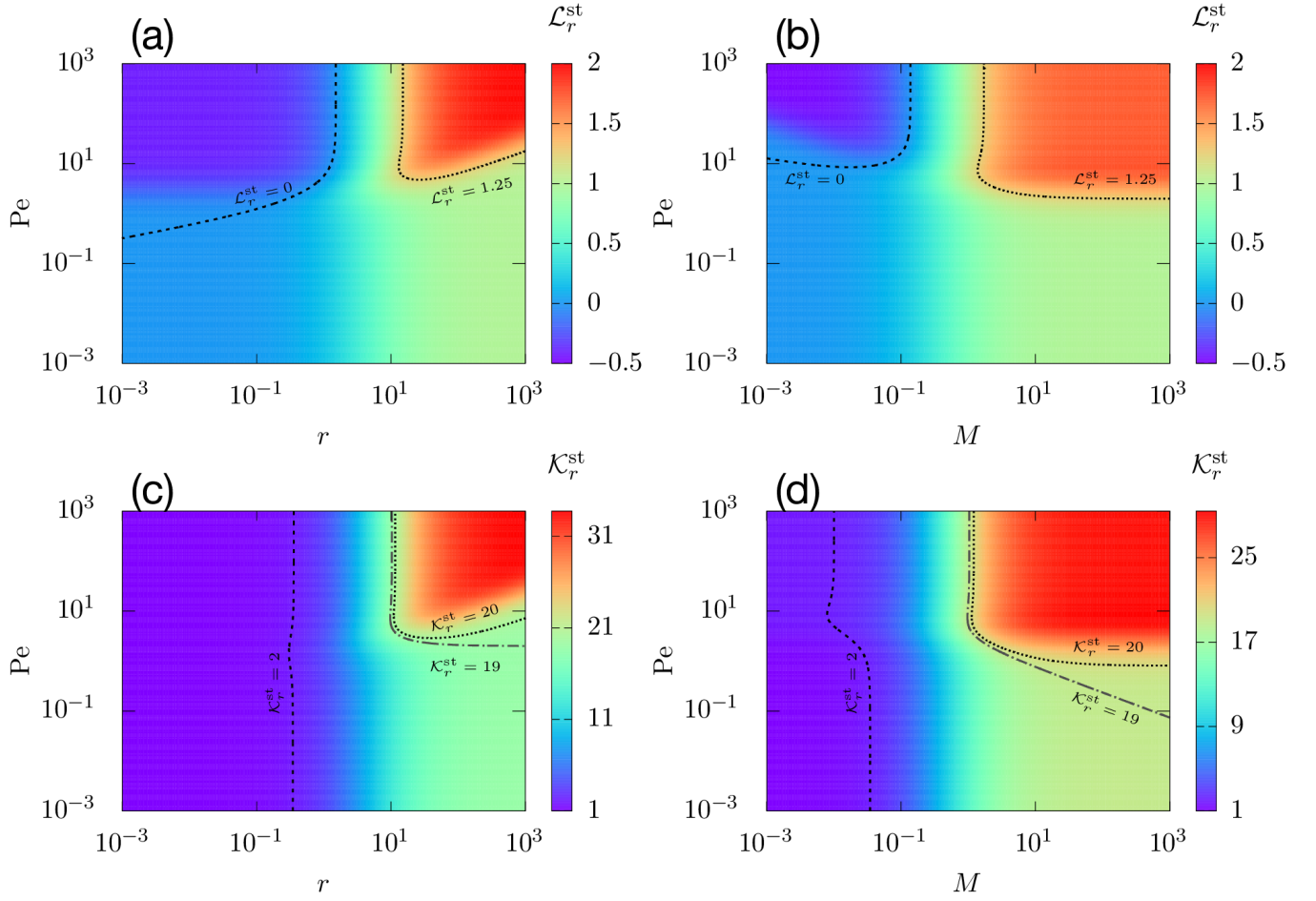


FIG. 6. Activity-controlled phase diagrams of steady-state excess kurtosis. Steady-state excess kurtosis of velocity, $\mathcal{L}_r^{\text{st}}$, shown in (a,b), and position, $\mathcal{K}_r^{\text{st}}$, shown in (c,d), demonstrating activity-induced deviations from Gaussian statistics. (a,c) show the dependence on reset rate r and activity Pe at fixed inertia $M = 1$, while (b,d) show the dependence on inertia M and activity Pe at fixed reset rate $r = 10$. Increasing activity drives a crossover from weakly non-Gaussian steady states to strongly non-Gaussian regimes, highlighting the growing influence of persistence and inertia in shaping reset-controlled steady-state fluctuations.